

Initial spin fluctuations as a probe of cluster spin structure in ^{16}O and ^{20}Ne nuclei

Xiang Fan,¹ Jun-Qi Tao,^{1,2} Ze-Fang Jiang,^{3,*} and Ben-Wei Zhang^{1,†}

¹*Institute of Particle Physics and Key Laboratory of Quark and Lepton Physics (MOE), Central China Normal University, Wuhan, Hubei, 430079, China*

²*School of Science and Engineering, The Chinese University of Hong Kong, Shenzhen (CUHK-Shenzhen), Guangdong, 518172, China*

³*Department of Physics and Electronic-Information Engineering, Hubei Engineering University, Xiaogan, Hubei, 432000, China*

(Dated: January 1, 2026)

We investigate the imprint of α clustering on initial spin fluctuations in relativistic $^{16}\text{O} + ^{16}\text{O}$ and $^{20}\text{Ne} + ^{20}\text{Ne}$ collisions at $\sqrt{s_{\text{NN}}} = 5.36$ TeV. Utilizing *ab initio* configurations from Nuclear Lattice Effective Field Theory (NLEFT) and phenomenological α -cluster models within a Monte-Carlo Glauber framework, we compute the event-by-event variance of the initial net spin polarization. We find that the strong short-range spin-isospin correlations characteristic of α clusters lead to a significant suppression of spin fluctuations compared to a spherical Woods-Saxon baseline with uncorrelated spins. By constructing a scaled fluctuation observable that accounts for trivial finite-size effects, we demonstrate that this suppression exhibits a non-monotonic centrality dependence sensitive to the detailed cluster geometry. Furthermore, we propose the ratio of scaled spin fluctuations between ^{20}Ne and ^{16}O systems as a robust probe. Our results predict distinct percent-level deviations from the baseline for clustered nuclei, suggesting that measurements of final-state Λ -hyperon spin correlations can provide novel constraints on the ground-state spin structure of light nuclei.

I. INTRODUCTION

Relativistic heavy-ion collisions at RHIC and the LHC create strongly interacting QCD matter at extreme temperature, vorticity, and magnetic fields, commonly referred to as the quark-gluon plasma (QGP) [1, 2]. The observation of a global Λ -hyperon polarization in non-central heavy-ion collisions [3, 4] — in agreement with early theoretical predictions of spin-orbit coupling in the QGP [5, 6] — has opened a new avenue to study the spin degrees of freedom of the QGP at high energies. The overall magnitude and beam-energy dependence of the global Λ polarization are reasonably described by several hydrodynamic and transport models [7–9], improving our understanding of spin-orbit coupling and the vortical nature of the QGP fluid. At the same time, the so-called “sign puzzle” in local Λ polarization measurements — where the measured azimuthal dependence of the longitudinal polarization is opposite to theoretical expectations — has prompted renewed discussions about the origin and transport of spin in the QGP [10–12].

More recently, attention has shifted from event-averaged polarization to spin fluctuations and spin correlations [13–16]. On the theory side, Λ pair spin correlators have been formulated as sensitive probes of initial spin-density fluctuations, short-range spin-isospin correlations, and even quantum entanglement in the hyperon sector [17–21]. Experimentally, first measurements of hyperon pair spin correlations at RHIC demonstrate that such observables are accessible with good precision and already begin to constrain scenarios for spin transport and nontrivial quantum correlations in QCD matter [22].

At the same time, collisions of a growing variety of nuclear species (including ^{238}U , ^{129}Xe , ^{96}Ru , ^{96}Zr , ^{208}Pb , ^{20}Ne , and ^{16}O) have opened up the possibility of imaging nuclear structure with high-energy data [23–30]. In particular, light self-conjugate $N = Z$ nuclei such as ^{16}O and ^{20}Ne are known to exhibit pronounced α -cluster structures, a phenomenon well-established by a long history of low-energy nuclear experiments and phenomenological studies [31–33]. From a first-principles perspective, these clustering correlations are successfully described by modern *ab initio* frameworks, including Quantum Monte Carlo methods [34], the No-Core Shell Model [35], Lattice Effective Field Theory [36, 37], and advanced generator coordinate methods [38]. Dedicated runs of $^{16}\text{O} + ^{16}\text{O}$ and $^{20}\text{Ne} + ^{20}\text{Ne}$ collisions at $\sqrt{s_{\text{NN}}} = 5.36$ TeV at the LHC therefore provide a unique opportunity to probe α clustering in a new, high-temperature regime [39, 40].

G. Giacalone and E. Speranza [17] has recently proposed a new paradigm relating initial-state spin fluctuations in the colliding nuclei to final-state spin correlations of emitted hadrons via relativistic spin hydrodynamics [41–44], introducing a frame-independent Λ -pair angular correlation observable v_{Λ}^2 as a direct experimental handle [13]. Within this framework, the variance of the event-by-event net polarization of the fireball is approximately preserved during the hydrodynamic evolution and can be accessed experimentally through measurements of v_{Λ}^2 . This opens up the possibility of probing ground-state nuclear spin structure in high-energy collisions. However, to date, this idea has not been applied to investigate special nuclear ground-state spin structures such as those arising from α clustering.

Motivated by these developments, in the present work we investigate how α -cluster-induced spin structures in ^{16}O and ^{20}Ne are imprinted on the initial spin fluctuations in ultra-relativistic nucleus-nucleus collisions. A characteristic feature of α clustering is that within each $2p-2n$ cluster, spin and isospin combine to form an approximate spin-isospin singlet,

* jiangzf@mails.ccnu.edu.cn

† bwzhang@mail.ccnu.edu.cn

leading to strong local cancellation of nucleon spins and, consequently, to short-range spin-spin anti-correlations in the nuclear many-body wave function [45–47]. We show that these microscopic correlations lead to a suppression of the standard deviation $\sqrt{\langle \mathcal{P}^2 \rangle}$ of the initial net polarization (event by event) compared to a spherical Woods-Saxon baseline with uncorrelated nucleon spins. By introducing a suitably scaled polarization fluctuation that removes the trivial finite-size effect associated with the total spin $J = 0$ of each nucleus, we demonstrate that cluster-induced spin structures produce characteristic dependencies on collision centrality and system size that can serve as quantitative experimental probes of α clustering. In particular, we propose the ratio of the scaled polarization fluctuation between $^{20}\text{Ne} + ^{20}\text{Ne}$ and $^{16}\text{O} + ^{16}\text{O}$ collisions as a robust observable to discriminate between different α -cluster configurations and to constrain *ab initio* nuclear structure calculations.

The paper is organized as follows. In Sec. II we summarize the theoretical framework that relates initial spin fluctuations to final-state Λ -pair observables, describe the nuclear-structure inputs for ^{16}O and ^{20}Ne , and define the relevant observables. Section III presents our numerical results for $^{16}\text{O} + ^{16}\text{O}$ and $^{20}\text{Ne} + ^{20}\text{Ne}$ collisions at $\sqrt{s_{\text{NN}}} = 5.36$ TeV. In Sec. IV we summarize our findings and discuss their implications for future theoretical and experimental studies.

II. METHOD

In this section, we outline the framework for probing initial spin fluctuations. We first introduce the theoretical framework connecting initial spin fluctuations to final-state spin polarization observables. Then, we describe the initial nuclear structure inputs for ^{16}O and ^{20}Ne , starting from *ab initio* lattice effective field theory (NLEFT) configurations, followed by α -cluster models, and a 3pf Woods-Saxon distribution. Finally, we define the key observables: the standard deviation $\sqrt{\langle \mathcal{P}^2 \rangle}$ of the initial spin polarization, the scaled standard deviation $\sqrt{\langle \mathcal{P}^2 \rangle}_{\text{scaled}}$, and the ratio of scaled standard deviations between different collision systems.

A. Initial spin fluctuations and final-state observables

In this subsection, the framework of Ref. [17], which connects initial spin fluctuations to measurable final-state observables, is summarized and adapted to the present study. The construction proceeds in three steps: (i) a stochastic model for the initial spin density and the associated event polarization, (ii) the definition of a frame-independent observable based on Λ -pair spin correlations, and (iii) the discussion of spin hydrodynamics, which provides the space-time evolution.

Initial spin density and event polarization. The starting point is an initial-condition model that provides, event by event, the transverse distribution of participant nucleons and the corresponding spin density at midrapidity. Following Ref. [17], the initial spin density is encoded in a scalar field S

and a unit vector n^i specifying the orientation of the polarization,

$$S^i \equiv n^i S \quad [\hbar/\text{fm}^3], \quad (1)$$

and an initial spin density per unit rapidity at midrapidity is defined as

$$\lim_{\tau \rightarrow 0^+} \tau S = S(\mathbf{x}) \quad [\hbar/\text{fm}^2]. \quad (2)$$

In the present analysis the transverse distribution of participants is taken from the TRNTo model [48–50], and $S(\mathbf{x})$ is implemented in a Glauber-type form [51, 52] as

$$\mathcal{S}(\mathbf{x}) \equiv S_0 \frac{\hbar}{2} \sum_{i=1}^{N_{\text{part}}} s_i w_s(\mathbf{x} - \mathbf{x}_i), \quad (3)$$

where \mathbf{x} is the transverse coordinate, \mathbf{x}_i denotes the position of the i -th participant, w_s is a normalized smearing profile, $s_i = \pm 1$ is a spin projection along a quantization axis, and S_0 is a dimensionless normalization parameter. The orientation of the quantization axis is chosen randomly and independently in each event, such that the ensemble of events is globally unpolarized.

Integrating $\mathcal{S}(\mathbf{x})$ over the transverse plane gives the net spin carried by the participants in that event. It is convenient to characterize the corresponding fluctuating polarization through the dimensionless event variable

$$\mathcal{P}_{\text{ini}} = \frac{1}{N_{\text{part}}} \sum_{i=1}^{N_{\text{part}}} s_i, \quad -1 \leq \mathcal{P}_{\text{ini}} \leq 1. \quad (4)$$

Because the colliding nuclei have total spin $J = 0$ and the quantization axis is randomized from event to event, the mean polarization vanishes, $\langle \mathcal{P}_{\text{ini}} \rangle = 0$, whereas the variance $\langle \mathcal{P}_{\text{ini}}^2 \rangle$ is nonzero and measures the size of initial spin fluctuations. The field $\mathcal{S}(\mathbf{x})$ therefore provides a well-defined initial spin density profile that can serve as input for spin hydrodynamics, while \mathcal{P}_{ini} encodes the associated event-wise net polarization.

Λ -pair spin correlations. The direction of \mathcal{P}_{ini} in spin space is random from event to event. As a consequence, the global polarization of produced hadrons measured with respect to a fixed laboratory axis vanishes after event averaging, and observables that are linear in the polarization are blind to the fluctuations of interest. One therefore needs an observable that is sensitive to \mathcal{P}^2 rather than to \mathcal{P} itself.

Ref. [17] proposed to access initial spin fluctuations via spin correlations of pairs of Λ hyperons reconstructed in the final state. Owing to the parity-violating weak decay $\Lambda \rightarrow p\pi^-$, the distribution of the decay proton direction $\hat{\mathbf{p}}_p$ in the Λ rest frame is correlated with the Λ polarization vector \mathbf{P} as

$$\frac{dN}{d\Omega_p} \propto 1 + \alpha_{\Lambda} \mathbf{P} \cdot \hat{\mathbf{p}}_p, \quad (5)$$

where α_{Λ} is the weak-decay parameter [53] and $d\Omega_p$ is the solid angle of $\hat{\mathbf{p}}_p$. An analogous relation holds for anti-hyperons $\bar{\Lambda} \rightarrow \bar{p}\pi^+$ with decay parameter $\alpha_{\bar{\Lambda}} \simeq -\alpha_{\Lambda}$.

This relation forms the basis of hyperon-polarization measurements in heavy-ion collisions [3].

In a given event we consider pairs of (anti)hyperons, labeled 1 and 2, which can be of the type $\Lambda\Lambda$, $\Lambda\bar{\Lambda}$, or $\bar{\Lambda}\bar{\Lambda}$. Their decay (anti)protons define two unit vectors $\hat{\mathbf{p}}_{p,1}$ and $\hat{\mathbf{p}}_{p,2}$ in the respective rest frames, and we denote by

$$\cos \Delta\theta \equiv \hat{\mathbf{p}}_{p,1} \cdot \hat{\mathbf{p}}_{p,2} \quad (6)$$

the cosine of the relative angle between them. By averaging $\cos \Delta\theta$ over all hyperon pairs and events in a given centrality class and normalizing by the appropriate weak-decay parameters α_1 and α_2 of the two hyperons in the pair, one defines the frame-independent correlator

$$v_\Lambda^2 \equiv \frac{9}{\alpha_1 \alpha_2} \langle\langle \cos \Delta\theta \rangle\rangle, \quad (7)$$

where the double brackets denote a pair and event average. In practice, α_1 and α_2 are taken as the corresponding decay parameters of each hyperon in the pair, so that the same definition applies uniformly to $\Lambda\Lambda$, $\Lambda\bar{\Lambda}$, and $\bar{\Lambda}\bar{\Lambda}$ pairs.

This construction is directly analogous to methods employed in other areas of high-energy physics, where angular correlations of decay products are used to probe underlying spin entanglement, such as in top–antitop pair production at the LHC [13, 54, 55].

Under the assumptions of Ref. [17]—namely that in each event all hyperons share a common polarization vector \mathbf{P} , whose orientation is random from event to event, and that non-flow correlations between different hyperons are negligible—the observable v_Λ^2 reduces to the variance of the event-wise net polarization in the final state,

$$v_\Lambda^2 = \langle \mathcal{P}^2 \rangle_{\text{final}}. \quad (8)$$

A detailed derivation of Eq. (8), starting from the joint angular distribution of the two decay protons and the spin-correlation matrix, is given in Appendix A. In our framework v_Λ^2 is thus the experimental counterpart of the initial polarization variance $\langle \mathcal{P}_{\text{ini}}^2 \rangle$ generated by different nuclear spin structures.

Spin hydrodynamics and connection to initial fluctuations. The space–time evolution of the quark–gluon plasma with spin degrees of freedom is described by relativistic spin hydrodynamics [41, 43, 56], whose equations of motion for an uncharged fluid are governed by the conservation of energy–momentum and of the spin tensor $S^{\lambda,\mu\nu}$,

$$\partial_\mu T^{\mu\nu} = 0, \quad \partial_\lambda S^{\lambda,\mu\nu} = 0, \quad (9)$$

where $T^{\mu\nu}$ is the energy–momentum tensor and $S^{\lambda,\mu\nu}$ is antisymmetric in the last two indices. Different pseudo-gauge choices correspond to different decompositions of orbital and spin angular momentum, but leave the total conserved charges unchanged [57, 58]. Following Ref. [17], one can define from $S^{\lambda,\mu\nu}$ a spin-density four-vector S^μ and relate its spatial components to the scalar field $S(\mathbf{x})$ introduced above. Details of this construction, as well as the explicit mapping between $S^{\lambda,\mu\nu}$ and the initial density $S(\mathbf{x})$, are summarized in Appendix B.

In the regime relevant for ultra-relativistic nucleus–nucleus collisions, Ref. [17] assumes that the total spin of the fireball is approximately conserved during the hydrodynamic evolution and that spin diffusion is moderate. Under this assumption the magnitude of the event polarization is essentially preserved from the initial to the final state, so that

$$\langle \mathcal{P}^2 \rangle_{\text{final}} \simeq \langle \mathcal{P}_{\text{ini}}^2 \rangle. \quad (10)$$

In the present study the full spin-hydrodynamic evolution is not simulated explicitly; instead, our attention is focused on the initial polarization fluctuations generated by different microscopic nuclear structures, encoded in $\langle \mathcal{P}_{\text{ini}}^2 \rangle$ and in its scaled version, while residual dynamical effects from spin transport are expected to affect collision systems with similar mass numbers in a similar way. Consequently, when ratios of observables between systems, such as the system-size ratio introduced below, are formed, a large part of the dynamical attenuation is expected to cancel, leaving a cleaner sensitivity to the underlying nuclear spin structure.

B. Nuclear structure inputs

To investigate how nuclear structure affects initial spin fluctuations, we focus on the spin structure of the ground states of ^{16}O and ^{20}Ne . To construct initial conditions for spin hydrodynamics, the model must specify, on an event-by-event basis, both the spatial coordinates and the spin of all nucleons. ^{16}O and ^{20}Ne belong to the class of self-conjugate $4n$ light nuclei, for which mean-field descriptions are known to be strongly modified by the formation of spatially localized α clusters [31–33]. A characteristic feature of such clustering is that, inside each α particle, the spins and isospins of the four nucleons combine into (approximately) spin–isospin singlet configurations [45–47], leading to strong local cancellation of spin and, consequently, pronounced short-range spin–spin anti-correlations in the nuclear many-body wave function. To explore how these correlations are imprinted on the initial spin polarization, the model assigns to each nucleon a spatial position \mathbf{x}_i and a spin projection $s_i = \pm 1$, and employs three distinct types of nuclear-structure input: *ab initio* configurations, explicit α -cluster models, and a baseline 3pf Woods–Saxon distribution without clustering.

Ab initio NLEFT configurations. For ^{16}O and ^{20}Ne we employ microscopic configurations generated within Nuclear Lattice Effective Field Theory (NLEFT) [36, 59]. NLEFT solves the nuclear A -body problem on a spacetime lattice using chiral effective field theory interactions, and, in particular, the pinhole algorithm allows one to sample the A -body density in both coordinate and spin–isospin space [60, 61]. In this work we use the ^{16}O and ^{20}Ne pinhole configurations reported in Refs. [60, 61]. These configurations provide, for each Monte-Carlo event, the full set of nucleon positions together with their spin–isospin quantum numbers, so that correlations between positions and spins, including higher-order many-body correlations, are preserved and can be directly mapped to the initial conditions of our spin-hydrodynamic model.

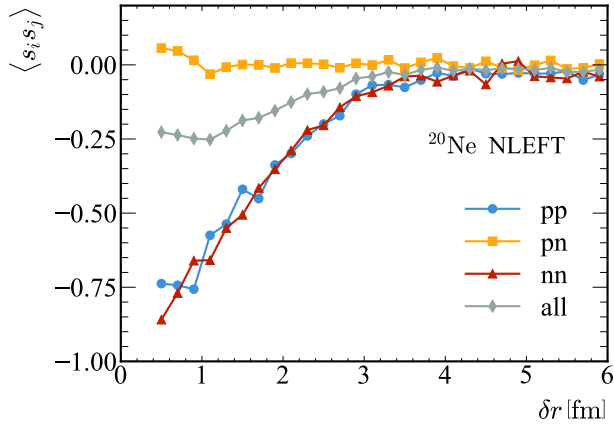


FIG. 1. (Color online) Two-nucleon spin correlation $\langle s_i s_j \rangle$ as a function of the relative distance δr in ^{20}Ne from *ab initio* NLEFT calculations. The blue circles, yellow squares, red triangles, and gray diamonds represent $\langle s_i s_j \rangle(\delta r)$ for proton–proton, proton–neutron, neutron–neutron, and all nucleon pairs, respectively.

The microscopic spin structure captured by NLEFT is illustrated in Fig. 1, which shows the two-nucleon spin correlation $\langle s_i s_j \rangle$ as a function of relative distance δr in ^{20}Ne . In practice, $\langle s_i s_j \rangle(\delta r)$ is obtained by taking, for each NLEFT configuration, the product $s_i s_j$ of all nucleon pairs, binning them according to their separation $\delta r = |\mathbf{x}_i - \mathbf{x}_j|$, and then averaging over the ensemble of configurations. A distinct pattern is observed: for like-particle pairs (proton–proton and neutron–neutron), the spin correlation is negative at short distances ($\delta r \lesssim 3$ fm) and vanishes at larger distances. This reflects the Pauli exclusion principle and the tendency of identical nucleons to pair with opposite spins within compact clusters. Conversely, the proton–neutron correlation remains negligible across all distances. This specific short-range antiferromagnetic-like ordering is consistent with the expected α -cluster structure of ^{20}Ne , which strongly deviates from uncorrelated mean-field densities, see, e.g., Refs. [62, 63].

Explicit α -cluster models.

To systematically study the influence of geometry and spin suppression, we adopt phenomenological α -cluster models that have been shown to reproduce one-body densities of ^{16}O and ^{20}Ne obtained from modern *ab initio* calculations. Following the Gaussian cluster framework of Ref. [64], each nucleus is composed of N_α independent α particles. The spatial distribution of nucleons within each cluster i is sampled from a Gaussian profile,

$$\rho_\alpha(\mathbf{x}) \propto \exp \left[-\frac{3(\mathbf{x} - \mathbf{L}_i)^2}{2r_L^2} \right], \quad (11)$$

where \mathbf{L}_i is the center of the i -th cluster and r_L is the root mean-square radius of cluster (RMS). To mimic the $J = 0$ ground state, we enforce strict spin–isospin cancellation within each cluster: each α cluster consists of two protons and two neutrons, with spins strictly anti-aligned ($\uparrow\downarrow$) for each

TABLE I. Nuclear-structure parameters used in this work. The upper part lists the α -cluster model parameters (r_L, ℓ_c, ℓ_h) in fm for ^{16}O and ^{20}Ne , adopted from the χ^2 fits of Ref. [64] to NLEFT, PGCM, VMC and 3pf densities. The lower part summarizes the parameters of the three-parameter Fermi (3pf) Woods–Saxon distributions and of the schematic $^{16}\text{O} + \alpha$ configuration.

Nucleus / Model	Reference Density	r_L (fm)	ℓ_c (fm)	ℓ_h (fm)
^{16}O (tetrahedron)	NLEFT	1.84	3.17	–
	PGCM	1.88	3.06	–
	VMC	1.52	3.26	–
^{20}Ne (bowling–pin)	NLEFT	2.20	3.00	3.50
Nucleus / Model	R (fm)	a (fm)	w	d_1 (fm)
^{16}O (3pf)	2.608	0.513	-0.051	–
^{20}Ne (3pf)	2.791	0.698	-0.168	–
^{20}Ne ($^{16}\text{O} + \alpha$)	2.608	0.513	-0.051	3.0
				2.164

isospin pair, resulting in zero net spin per cluster.

For the geometry, we consider structures that are consistent with both low-energy α -cluster models [65] and recent applications to relativistic collisions [64, 66], as illustrated in Fig. 2:

- **^{16}O (tetrahedron):** Four α clusters are arranged at the vertices of a regular tetrahedron with side length ℓ_c .
- **^{20}Ne (bowling–pin):** Modeled as a ^{16}O tetrahedral core plus an additional α cluster. This forms a distorted bi-pyramidal or “bowling–pin” shape, characterized by the core size ℓ_c and the distance ℓ_h of the fifth cluster from the core center.

In practice, we do not refit the cluster parameters in this work. Instead, we take over the parameter sets (r_L, ℓ_c, ℓ_h) obtained in Ref. [64], where they were determined by minimizing a χ^2 function to reproduce the one-body nucleon densities of NLEFT, VMC, PGCM and of a three-parameter Fermi (3pf) reference density for ^{16}O and ^{20}Ne . The resulting values for the configurations used in this study are collected in Tab I.

In addition to these pure α -cluster geometries, we also consider a schematic $^{16}\text{O} + \alpha$ configuration for ^{20}Ne , motivated by the $^{16}\text{O} + \alpha$ structures discussed in Refs. [65, 66]. In this case, a spherical ^{16}O core is generated from a 3pf Woods–Saxon distribution and a single α cluster with RMS r_L is attached at a fixed distance d_1 along a random direction in space. The parameters of the α -cluster models, of the 3pf Woods–Saxon nuclei, and of the $^{16}\text{O} + \alpha$ configuration are collected in TABLE I.

3pf Woods–Saxon baseline. As a baseline for comparison, we also employ spherical three-parameter Fermi (3pf) Woods–Saxon charge-density distributions. The radial density is taken as

$$\rho(r) = \rho_0 \frac{1 + w \left(\frac{r}{R} \right)^2}{1 + \exp \left(\frac{r - R}{a} \right)}, \quad (12)$$

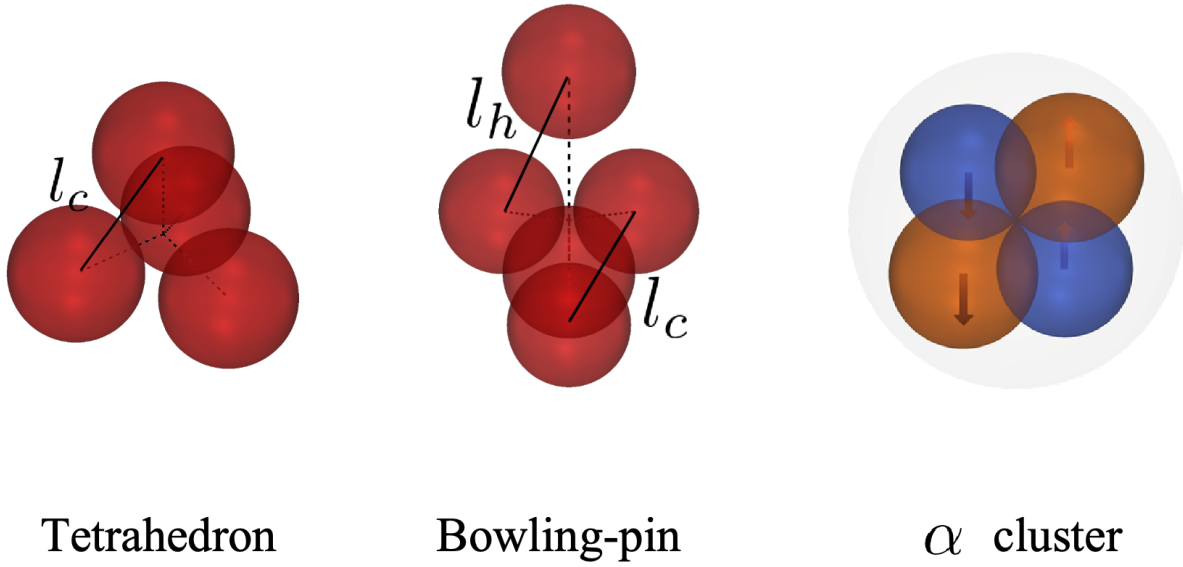


FIG. 2. Schematic illustration of the α -cluster geometries implemented in the model. (Left) The Tetrahedron configuration of ^{16}O is characterized by the α -cluster edge length ℓ_c . (Middle) The Bowling-pin configuration of ^{20}Ne is characterized by the core parameter ℓ_c and the distance ℓ_h between the fifth cluster and the core. (Right) A schematic of the α cluster, which contains two protons (orange spheres) and two neutrons (blue spheres). The directions of the black arrows ($\uparrow\downarrow$) in the right panel indicate the spin orientations of the individual nucleons. The spins of the two protons cancel each other out, as do the spins of the two neutrons, resulting in a net-zero spin for the cluster. Each red sphere in the geometry plots (Left and Middle) represents an α cluster.

where R is the half-density radius, a is the surface diffuseness, w controls a possible central depression of the density, and ρ_0 is fixed by the normalization to the mass number A . For ^{16}O and ^{20}Ne we use the standard 3pf parameter sets extracted from elastic electron-scattering data in Ref. [67]. In this model, nucleon positions are sampled from the smooth mean-field density $\rho(r)$ without any geometric clustering, and spins are assigned randomly (+1 or -1). This serves as a null hypothesis in which no intrinsic spin–position correlations are present.

C. Observables: spin fluctuations, baseline, and scaled observables

To quantify the imprint of nuclear structure on spin observables, we link the initial polarization fluctuations to the microscopic many-body density of the colliding nuclei. For detailed derivation, please refer to the Appendix C.

Net polarization and spin densities. The event-by-event net polarization \mathcal{P} is defined as the average spin of all participants,

$$\mathcal{P} = \frac{1}{N_{\text{part}}} \left(\sum_{i=1}^{N_{\text{part}}^A} s_{i,A} + \sum_{j=1}^{N_{\text{part}}^B} s_{j,B} \right), \quad (13)$$

where $s_{i,A} = \pm 1$ and $s_{j,B} = \pm 1$ denote the spin projections

of participants from nuclei A and B , and $N_{\text{part}} = N_{\text{part}}^A + N_{\text{part}}^B$. For unpolarized colliding ions one has $\langle s_{i,A} \rangle = \langle s_{j,B} \rangle = 0$, hence $\langle \mathcal{P} \rangle = 0$.

Assuming that spin degrees of freedom in the two nuclei are independent, the variance $\langle \mathcal{P}^2 \rangle$ can be expressed in terms of one- and two-body spin densities in each nucleus. For a system with N participants this dependence can be schematically written as

$$\langle \mathcal{P}^2 \rangle \propto N \sum_s \rho^{(1)}(s) s^2 + N(N/2-1) \sum_{s_1, s_2} \rho^{(2)}(s_1, s_2) s_1 s_2, \quad (14)$$

where $\rho^{(1)}$ and $\rho^{(2)}$ denote, respectively, the one- and two-body spin densities of the participants. The first term encodes the trivial variance of independent spins, while the second term is sensitive to genuine two-body spin–spin correlations, such as those induced by α clustering. A detailed derivation of Eq. (14) is collected in Appendix C.

Baseline from the $J = 0$ ground state. Even in the absence of clustering, the $J = 0$ ground state of a light nucleus imposes a global constraint $\sum_{i=1}^{A_{\text{mass}}} s_i = 0$, which leads to a uniform negative background correlation between any pair of nucleons. For a nucleus with mass number A_{mass} one finds (see Appendix C)

$$c = \langle s_i s_j \rangle_{\text{base}} = -\frac{1}{A_{\text{mass}} - 1}, \quad i \neq j, \quad (15)$$

which reflects the trivial anti-correlation required by the total spin singlet.

Assuming that this background correlation characterizes all same-nucleus pairs, the corresponding baseline variance of the polarization in a collision between nuclei A and B is

$$\langle \mathcal{P}^2 \rangle_{\text{base}} = \frac{1}{N_{\text{part}}^2} \left[N_{\text{part}} + c N_{\text{part}} (N_{\text{part}}/2 - 1) \right], \quad (16)$$

By construction, $\langle \mathcal{P}^2 \rangle_{\text{base}}$ contains only the global $J = 0$ constraint and no additional local structure.

Scaled spin fluctuations and system-size ratio. Since $\langle \mathcal{P} \rangle = 0$, the standard deviation of the event-wise polarization is simply

$$\text{std}(\mathcal{P}) = \sqrt{\langle \mathcal{P}^2 \rangle}. \quad (17)$$

To remove the finite-size suppression associated with the $J = 0$ ground state and isolate nontrivial spin structures, we define the scaled spin fluctuation as

$$(\sqrt{\langle \mathcal{P}^2 \rangle})_{\text{scaled}} \equiv \frac{\sqrt{\langle \mathcal{P}^2 \rangle}}{\sqrt{\langle \mathcal{P}^2 \rangle}_{\text{base}}}, \quad (18)$$

which equals unity for the baseline correlations of Eq. (16) and deviates from unity only in the presence of additional spin–spin structures, such as the local spin cancellation inside α clusters.

Finally, to compare different collision systems we introduce the central observable used in Sec. III, namely the ratio of scaled fluctuations between ${}^{20}\text{Ne} + {}^{20}\text{Ne}$ and ${}^{16}\text{O} + {}^{16}\text{O}$ collisions,

$$R_{{}^{20}\text{Ne}/{}^{16}\text{O}} \equiv \frac{(\sqrt{\langle \mathcal{P}^2 \rangle})_{\text{scaled}}^{{}^{20}\text{Ne} + {}^{20}\text{Ne}}}{(\sqrt{\langle \mathcal{P}^2 \rangle})_{\text{scaled}}^{{}^{16}\text{O} + {}^{16}\text{O}}}. \quad (19)$$

This ratio is designed to enhance the sensitivity to cluster-induced spin structures while reducing common-mode uncertainties in the overall normalization of the spin signal.

III. NUMERICAL RESULTS

In this section, we present numerical simulations of initial spin fluctuations in ${}^{16}\text{O} + {}^{16}\text{O}$ and ${}^{20}\text{Ne} + {}^{20}\text{Ne}$ collisions at $\sqrt{s_{\text{NN}}} = 5.36$ TeV, based on the framework outlined in Sec. II A. For each nuclear-structure model introduced in Sec. II B, we generate a large ensemble of TRENTO events, compute the event-wise polarization \mathcal{P} , and study both the standard deviation $\sqrt{\langle \mathcal{P}^2 \rangle}$ and the scaled quantity $(\sqrt{\langle \mathcal{P}^2 \rangle})_{\text{scaled}}$ defined in Sec. II C. In addition, we analyze the system-size ratio of the scaled fluctuations between ${}^{20}\text{Ne} + {}^{20}\text{Ne}$ and ${}^{16}\text{O} + {}^{16}\text{O}$ collisions, which provides a more robust probe of differences in the underlying spin structure. The results are shown as a function of centrality, which is determined from the total entropy in TRENTO [48, 49], in analogy with Ref. [17].

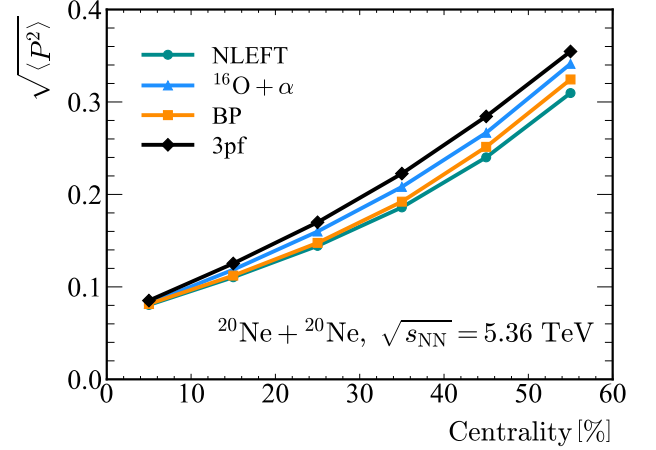


FIG. 3. (Color online) Standard deviation of the polarization parameter $\sqrt{\langle \mathcal{P}^2 \rangle}$ as a function of centrality in ${}^{20}\text{Ne} + {}^{20}\text{Ne}$ collisions at $\sqrt{s_{\text{NN}}} = 5.36$ TeV for different nuclear-structure configurations. The green circles, blue triangles, orange squares, and black diamonds correspond to the NLEFT, ${}^{16}\text{O} + \alpha$, BP, and spherical 3pf Woods–Saxon configurations, respectively.

As a baseline for comparison, we employ 3pf Woods–Saxon distributions for both systems. In this case, nucleon spins are completely uncorrelated in position space, and the only constraint comes from the overall $J = 0$ quantum number of the ground state. Deviations from this 3pf Woods–Saxon baseline therefore directly quantify nontrivial spin–spin correlations induced by cluster structures.

A. ${}^{20}\text{Ne} + {}^{20}\text{Ne}$ collisions

Fig. 3 displays the centrality dependence of $\sqrt{\langle \mathcal{P}^2 \rangle}$ in ${}^{20}\text{Ne} + {}^{20}\text{Ne}$ collisions for four different nuclear configurations: the *ab initio* NLEFT configurations, the bowling-pin (BP) 5α cluster model fitted to NLEFT, the ${}^{16}\text{O} + \alpha$ cluster configuration, and the spherical 3pf Woods–Saxon distribution.

For all centralities, the 3pf Woods–Saxon case yields the largest $\sqrt{\langle \mathcal{P}^2 \rangle}$. Introducing α clustering systematically suppresses the fluctuation of the net spin. This suppression is strongest for the BP and NLEFT configurations, which both realize a compact 5α geometry with pronounced local spin cancellation. The ${}^{16}\text{O} + \alpha$ configuration shows an intermediate behavior: its $\sqrt{\langle \mathcal{P}^2 \rangle}$ curve lies below the 3pf Woods–Saxon baseline, but above the BP and NLEFT results, indicating that the detached α cluster at larger radius generates weaker short-range spin anti-correlations than the BP core with 5α clusters. These trends become more transparent after removing the trivial finite-size effect.

In Fig. 4 we show the scaled standard deviation $(\sqrt{\langle \mathcal{P}^2 \rangle})_{\text{scaled}}$. The 3pf Woods–Saxon curve fluctuates mildly around unity, confirming that our baseline construction effectively captures the negative background correlation

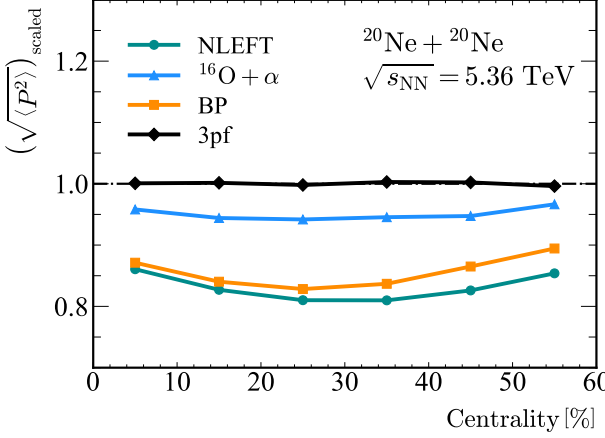


FIG. 4. (Color online) Centrality dependence of the scaled standard deviation of the polarization parameter $(\sqrt{\langle P^2 \rangle})_{\text{scaled}}$ in $^{20}\text{Ne} + ^{20}\text{Ne}$ collisions at $\sqrt{s_{\text{NN}}} = 5.36$ TeV. The teal circles, blue triangles, orange squares, and black diamonds correspond to the NLEFT, $^{16}\text{O} + \alpha$, BP, and spherical 3pf Woods–Saxon configurations, respectively. The horizontal dashed line indicates the reference value of unity.

induced solely by the $J = 0$ constraint. In contrast, all clusterized configurations yield $(\sqrt{\langle P^2 \rangle})_{\text{scaled}} < 1$ over the whole centrality range, demonstrating that cluster-induced local spin–spin anti-correlations further reduce the net-spin fluctuations beyond the global constraint.

The suppression is most pronounced at intermediate centralities where N_{part} is large enough to sample several clusters but not so large that the entire nucleus is fully overlapped. We observe a characteristic non-monotonic behavior: $(\sqrt{\langle P^2 \rangle})_{\text{scaled}}$ first decreases from central to mid-central collisions, reaches a minimum, and then increases again towards peripheral events. Physically, this pattern reflects the interplay between the number of independent α clusters participating in the collision and the efficiency of local spin cancellation within each cluster. The NLEFT and BP curves nearly coincide, indicating that the fitted BP geometry captures most of the spin-structure information contained in the NLEFT configurations for ^{20}Ne . By contrast, the $^{16}\text{O} + \alpha$ configuration remains closer to the 3pf Woods–Saxon reference, which suggests that measurements of $(\sqrt{\langle P^2 \rangle})_{\text{scaled}}$ in $^{20}\text{Ne} + ^{20}\text{Ne}$ collisions can discriminate between a genuine 5 α bowling-pin structure and a more loosely bound $^{16}\text{O} + \alpha$ configuration [62, 63, 66, 68].

B. $^{16}\text{O} + ^{16}\text{O}$ collisions

We now turn to $^{16}\text{O} + ^{16}\text{O}$ collisions. Fig. 5 shows $\sqrt{\langle P^2 \rangle}$ for the NLEFT configurations, for tetrahedral 4 α cluster models fitted to NLEFT, PGCM, and VMC densities, and for the spherical 3pf Woods–Saxon reference.

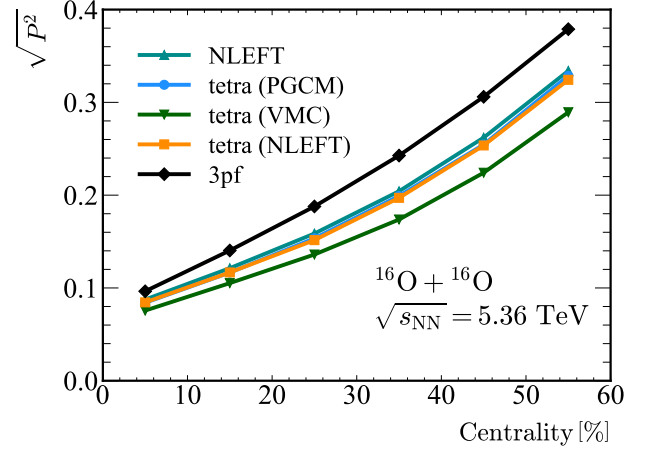


FIG. 5. (Color online) Standard deviation of the polarization parameter $\sqrt{\langle P^2 \rangle}$ as a function of centrality in $^{16}\text{O} + ^{16}\text{O}$ collisions at $\sqrt{s_{\text{NN}}} = 5.36$ TeV. Teal triangles show the *ab initio* NLEFT result. “tetra (PGCM)”, “tetra (VMC)”, and “tetra (NLEFT)” (blue circles, green downward triangles, and orange squares) are tetrahedral 4 α configurations fitted to PGCM, VMC, and NLEFT *ab initio* data, respectively, while “3pf” (black diamonds) denotes a spherical 3pf Woods–Saxon distribution.

As in the Neon (^{20}Ne) case, the 3pf Woods–Saxon distribution yields the largest spin fluctuations, while the presence of a tetrahedral 4 α geometry leads to a visible suppression of $\sqrt{\langle P^2 \rangle}$. The NLEFT initial states produce the smallest fluctuations, closely followed by the tetrahedral configurations fitted to NLEFT and PGCM densities. The VMC-based tetrahedron is slightly different, reflecting its more compact α clusters (smaller r_L) and/or modified intercluster distance ℓ_c . This confirms that $\sqrt{\langle P^2 \rangle}$ is sensitive not only to the existence of clustering, but also to the detailed geometry of the clusters encoded in the ratio r_L/ℓ_c [69, 70].

Fig. 6 presents the scaled observable, $(\sqrt{\langle P^2 \rangle})_{\text{scaled}}$, in $^{16}\text{O} + ^{16}\text{O}$ collisions at $\sqrt{s_{\text{NN}}} = 5.36$ TeV. Again, the 3pf Woods–Saxon curve stays close to unity, whereas all clusterized configurations give values below unity, with a centrality dependence similar to that observed in $^{20}\text{Ne} + ^{20}\text{Ne}$. The suppression is strongest at mid-central collisions, where the spectator region is still sizable but a large fraction of the tetrahedral structure participates in the interaction. Moreover, the three tetrahedral fits exhibit a clear ordering: the configuration with the most compact clusters (smallest r_L for a given ℓ_c) shows the largest deviation from the 3pf Woods–Saxon baseline. This demonstrates that $(\sqrt{\langle P^2 \rangle})_{\text{scaled}}$ is a quantitative probe of the underlying cluster spin structure, sensitive to subtle differences between modern *ab initio* descriptions of ^{16}O [30].

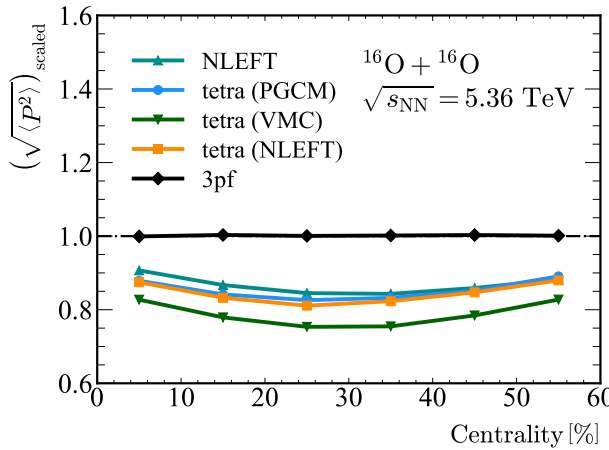


FIG. 6. (Color online) Centrality dependence of the scaled standard deviation of the polarization parameter $(\sqrt{\langle P^2 \rangle})_{\text{scaled}}$ in $^{16}\text{O} + ^{16}\text{O}$ collisions at $\sqrt{s_{\text{NN}}} = 5.36$ TeV. Teal triangles show the *ab initio* NLEFT result. The curves labeled “tetra (PGCM)”, “tetra (VMC)”, and “tetra (NLEFT)” (blue circles, green downward triangles, and orange squares) correspond to tetrahedral 4α configurations fitted to PGCM, VMC, and NLEFT *ab initio* data, respectively, while “3pf” (black diamonds) denotes a spherical 3pf Woods–Saxon distribution. The horizontal dashed line marks the reference value of unity.

C. System-size ratios and experimental prospects

While the scaled fluctuation already removes most of the trivial finite-size dependence, experimental measurements of $(\sqrt{\langle P^2 \rangle})_{\text{scaled}}$ in a single system may still suffer from residual systematic uncertainties and dynamical attenuation of the spin signal during the hydrodynamic evolution. To further suppress such effects, we consider the system-size ratio $R_{^{20}\text{Ne}/^{16}\text{O}}$, defined in Eq. (19), as presented in Fig. 7.

For spherical 3pf Woods–Saxon nuclei, the ratio is very close to unity over the entire centrality range. This confirms that, once the global $J = 0$ constraint is factored out, the remaining finite-size effects in $(\sqrt{\langle P^2 \rangle})_{\text{scaled}}$ are nearly identical in ^{16}O and ^{20}Ne . Consequently, deviations of $R_{^{20}\text{Ne}/^{16}\text{O}}$ from unity directly reflect differences in the spin structure of the two nuclei.

The *ab initio* NLEFT configurations yield a ratio that is slightly below one, deviating by a few percent from the 3pf Woods–Saxon baseline. In contrast, when both nuclei are modeled by simple cluster configurations fitted to NLEFT densities (BP-shaped ^{20}Ne and tetrahedral ^{16}O), the ratio lies slightly above unity and exhibits a weak increase with centrality, approaching values of the order of 1.02 in the most peripheral bins. The opposite sign of the deviation in these two NLEFT-based scenarios indicates that the minimal α -cluster models do not capture all the spin-structure information present in the full *ab initio* wave functions. In other words, the *ab initio* NLEFT configurations encode additional, more intricate spin–spin correlations beyond those associated

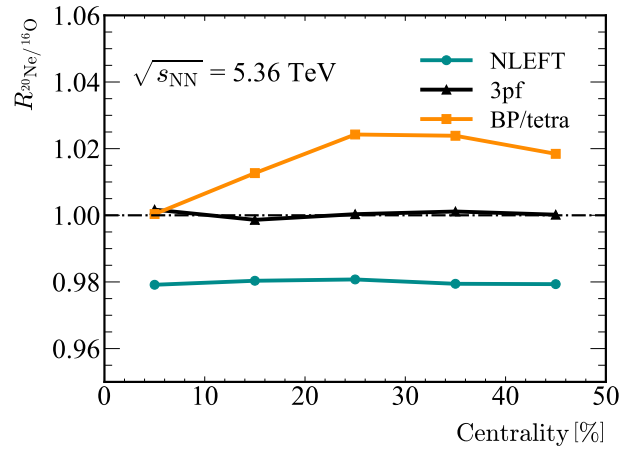


FIG. 7. (Color online) Centrality dependence of the ratio $R_{^{20}\text{Ne}/^{16}\text{O}}$ of the scaled standard deviation of the polarization parameter $(\sqrt{\langle P^2 \rangle})_{\text{scaled}}$ between $^{20}\text{Ne} + ^{20}\text{Ne}$ and $^{16}\text{O} + ^{16}\text{O}$ collisions at $\sqrt{s_{\text{NN}}} = 5.36$ TeV. Teal circles show the ratio obtained from *ab initio* NLEFT initial states, black triangles the ratio for spherical 3pf Woods–Saxon nuclei, and orange squares the ratio for BP-shaped ^{20}Ne and tetrahedral ^{16}O configurations fitted to NLEFT data.

with idealized α clusters.

From an experimental perspective, the pattern in Fig. 7 is particularly attractive. The 3pf Woods–Saxon ratio provides a robust reference close to unity, while realistic clustered nuclei produce deviations of order 2% that are roughly constant or slowly varying with centrality. Such percent-level differences are similar in magnitude to the initial-spin signals estimated for heavy systems in Ref. [17], and should be within reach of high-statistics $^{16}\text{O} + ^{16}\text{O}$ and $^{20}\text{Ne} + ^{20}\text{Ne}$ runs at the LHC. This ratio is designed to cancel residual system-size and hydrodynamic effects that are common to both collision systems, thereby isolating differences in their intrinsic spin structures. A combined measurement of $(\sqrt{\langle P^2 \rangle})_{\text{scaled}}$ in both systems, together with their ratio, would thus provide a new, spin-based probe of clustering in light nuclei that is complementary to traditional low-energy observables.

IV. SUMMARY AND OUTLOOK

In this work we have explored, for the first time, how the spin structure of light α -clustered nuclei affects initial spin fluctuations in ultra-relativistic nucleus–nucleus collisions within the theoretical framework that relates initial spin fluctuations to final-state Λ -pair spin correlations [17]. In particular, we focused on ^{16}O and ^{20}Ne , where the ground states are dominated by $2p-2n$ α clusters in which spin and isospin are locally cancelled, leading to pronounced short-range spin–spin anti-correlations. Our aim was to quantify how such microscopic correlations manifest themselves in the event-by-event fluctuations of the net spin polarization of the fireball.

As nuclear-structure input we employed *ab initio* configu-

lations from Nuclear Lattice Effective Field Theory (NLEFT), which provide for each event the full set of nucleon coordinates and spin quantum numbers, together with several phenomenological α -cluster geometries and spherical 3pf Woods–Saxon distributions without intrinsic spin–spin correlations. For each of these models we generated Monte-Carlo samples of $^{16}\text{O} + ^{16}\text{O}$ and $^{20}\text{Ne} + ^{20}\text{Ne}$ collisions at $\sqrt{s_{\text{NN}}} = 5.36$ TeV using the TRENTo framework, and evaluated both the standard deviation $\sqrt{\langle \mathcal{P}^2 \rangle}$ of the initial polarization and its scaled version that removes the trivial suppression associated with the finite number of participants and the $J = 0$ ground state. We find that 3pf Woods–Saxon nuclei exhibit the largest $\sqrt{\langle \mathcal{P}^2 \rangle}$, whereas clustered and NLEFT configurations show a significant suppression due to local spin–spin anti-correlations inside the α clusters. After scaling, all clustered configurations yield $(\sqrt{\langle \mathcal{P}^2 \rangle})_{\text{scaled}} < 1$ with a characteristic non-monotonic centrality dependence. The NLEFT results are closely reproduced by a bowling-pin 5α geometry for ^{20}Ne and by a tetrahedral 4α configuration for ^{16}O fitted to NLEFT densities, indicating that these simple models capture the main features of the underlying cluster spin structure.

Beyond this overall suppression, the scaled fluctuations are sensitive to the detailed cluster geometry. In $^{16}\text{O} + ^{16}\text{O}$ collisions, different tetrahedral configurations fitted to NLEFT, PGCM, and VMC densities exhibit a clear ordering that reflects the compactness of the clusters, encoded in the ratio r_L/ℓ_c . In $^{20}\text{Ne} + ^{20}\text{Ne}$ collisions, $(\sqrt{\langle \mathcal{P}^2 \rangle})_{\text{scaled}}$ distinguishes between a compact bowling-pin 5α structure and a more loosely bound $^{16}\text{O} + \alpha$ configuration. We further proposed the system-size ratio of scaled fluctuations, $R_{^{20}\text{Ne}/^{16}\text{O}}$, as a more robust observable. For 3pf Woods–Saxon nuclei this ratio stays very close to unity, providing a null hypothesis in which no special spin structure is present. In contrast, clustered nuclei produce percent-level deviations: for bowling-pin ^{20}Ne and tetrahedral ^{16}O fitted to NLEFT densities the ratio increases with centrality and reaches values of about 1.02 in more peripheral bins, while for full NLEFT configurations it remains slightly below one, around 0.98. The opposite sign of the deviation suggests that NLEFT contains more intricate spin–spin correlations than those encoded in minimal α -cluster models, underscoring the potential of $R_{^{20}\text{Ne}/^{16}\text{O}}$ as a sensitive probe of nuclear spin structure.

In summary, percent-level deviations of $R_{^{20}\text{Ne}/^{16}\text{O}}$ from unity would provide direct experimental evidence of nontrivial spin structures associated with α clustering in light nuclei.

Several extensions of the present study are worth pursuing. First, the initial spin density $\mathcal{S}(\mathbf{x})$ constructed here should be evolved within full relativistic spin hydrodynamics [44, 71] in order to quantify the dynamical attenuation of spin fluctuations from the initial state to the final-state Λ polarization. More realistic initial spin models, including spin transport during the early nucleon–nucleon scatterings and a construction of initial spin densities that is more closely tied to quantum-mechanical principles [72], would further improve the predictive power. Second, it will be interesting to extend the present analysis to other nuclear systems, such as isotopic pairs like ^{96}Ru and ^{96}Zr [73], which may help disentangle proton–proton, neutron–neutron, and proton–neutron spin correlations. Finally, additional *ab initio* inputs for light and medium-mass nuclei will allow one to better constrain first-principles descriptions of nuclear spin structure. The percent-level differences predicted here for $R_{^{20}\text{Ne}/^{16}\text{O}}$ should be within reach of future high-luminosity ^{16}O and ^{20}Ne runs at the LHC, offering a promising opportunity to test these ideas experimentally.

ACKNOWLEDGMENTS

We are grateful to Ulf-G. Meißner, Dean Lee, and Shihang Shen for providing the *ab initio* nuclear configurations from Nuclear Lattice Effective Field Theory (NLEFT) calculations. We especially thank Shihang Shen for preparing the specific datasets for ^{16}O and ^{20}Ne with spin information and for valuable discussions on their usage. We thank Giuliano Giacalone for inspiring this study and for enlightening discussions regarding the theoretical framework. We also appreciate helpful comments from Weiyao Ke. This work was supported by the National Natural Science Foundation of China (NSFC) under Grants No. 12305138 and No. 12535010, the Guangdong Major Project of Basic and Applied Basic Research under Grant No. 2020B0301030008, and the Xiaogan Natural Science Foundation under Grant No. XGKJ2023010063. X.F. acknowledges support from the China Scholarship Council (CSC).

[1] K. t. P. C. Adcox, Nucl. Phys. A **757**, 184 (2005).
[2] B. Müller, J. Schukraft, and B. Wyslouch, Ann. Rev. Nucl. Part. Sci. **62**, 361 (2012).
[3] L. t. S. C. Adamczyk, Nature **548**, 62 (2017).
[4] S. t. A. C. Acharya, Phys. Rev. C **101**, 044611 (2020).
[5] Z.-T. Liang and X.-N. Wang, Phys. Rev. Lett. **94**, 102301 (2005).
[6] F. Becattini, F. Piccinini, and J. Rizzo, Phys. Rev. C **77**, 024906 (2008).
[7] F. Becattini, I. Karpenko, M. A. Lisa, I. Upsal, and S. Voloshin, Phys. Rev. C **95**, 054902 (2017).
[8] Y. Xie, D. Wang, and L. P. Csernai, Phys. Rev. C **95**, 031901 (2017).
[9] H. Li, X.-L. Xia, X.-G. Huang, and H.-Z. Huang, Phys. Lett. B **820**, 136597 (2021), arXiv:2106.09443 [nucl-th].
[10] J. t. S. C. Adam, Phys. Rev. Lett. **123**, 132301 (2019).
[11] F. Becattini and I. Karpenko, Phys. Rev. Lett. **120**, 012302 (2018).
[12] X.-L. Xia, H. Li, X.-G. Huang, and H.-Z. Huang, Phys. Rev. C **100**, 014913 (2019).
[13] M. Baumgart and B. Tweedie, JHEP **03**, 117, arXiv:1212.4888 [hep-ph].
[14] M. Fucilla and Y. Hatta, (2025), arXiv:2509.05267 [hep-ph].
[15] Y. Afik, Y. Kats, J. R. M. de Nova, A. Soffer, and D. Uzan, Phys.

Rev. D **111**, L111902 (2025), arXiv:2406.04402 [hep-ph].

[16] T. Han, M. Low, N. McGinnis, and S. Su, JHEP **05**, 081, arXiv:2412.21158 [hep-ph].

[17] G. Giacalone and E. Speranza, (2025), arXiv:2502.13102 [nucl-th].

[18] L.-G. Pang, H. Petersen, Q. Wang, and X.-N. Wang, Phys. Rev. Lett. **117**, 192301 (2016).

[19] V. L. Lyuboshitz and V. V. Lyuboshitz, Phys. Part. Nucl. Lett. **7**, 370 (2010).

[20] J. Ellis and D. S. Hwang, JHEP **1011**, 026.

[21] S.-J. Lin, L.-G. Pang, and X.-N. Wang, JHEP In press.

[22] M. t. S. C. Abdallah, arXiv:2307.07373 [nucl-ex] (2023).

[23] M. I. Abdulhamid *et al.* (STAR), Nature **635**, 67 (2024), arXiv:2401.06625 [nucl-ex].

[24] J. Jia, Rept. Prog. Phys. **88**, 092301 (2025), arXiv:2501.16071 [nucl-th].

[25] G. Giacalone, G. Nijs, and W. van der Schee, Phys. Rev. Lett. **131**, 202302 (2023).

[26] B. Bally, G. Giacalone, and M. Bender, Phys. Rev. Lett. **128**, 082301 (2022).

[27] N. Summerfield, B.-N. Lu, C. Plumberg, D. Lee, J. Noronha-Hostler, and A. Timmins, Phys. Rev. C **104**, L041901 (2021), arXiv:2103.03345 [nucl-th].

[28] L.-M. Liu, H.-C. Wang, S.-J. Li, C. Zhang, J. Xu, Z.-Z. Ren, J. Jia, and X.-G. Huang, arXiv e-prints , arXiv:2502.08057 (2025), arXiv:2502.08057 [nucl-th].

[29] C. Ding, L.-G. Pang, S. Zhang, *et al.*, Chin. Phys. C **47**, 024105 (2023).

[30] C. Zhang, J. Chen, G. Giacalone, S. Huang, J. Jia, and Y.-G. Ma, Phys. Lett. B **862**, 139322 (2025), arXiv:2404.08385 [nucl-th].

[31] L. R. Hafstad and E. Teller, Phys. Rev. **54**, 681 (1938).

[32] K. Ikeda, N. Takigawa, and H. Horiuchi, Prog. Theor. Phys. Suppl. **68**, 464 (1968).

[33] M. Freer, H. Horiuchi, P. Schuck, and E. Tursunov, Rev. Mod. Phys. **90**, 035004 (2018).

[34] J. Carlson, S. Gandolfo, F. Pederiva, S. C. Pieper, R. Schiavilla, K. E. Schmidt, and R. B. Wiringa, Rev. Mod. Phys. **87**, 1067 (2015).

[35] B. R. Barrett, P. Navrátil, and J. P. Vary, Prog. Part. Nucl. Phys. **69**, 131 (2013).

[36] D. Lee, Prog. Part. Nucl. Phys. **63**, 117 (2009).

[37] E. Epelbaum, H. Krebs, D. Lee, and U.-G. Meißner, Phys. Rev. Lett. **106**, 192501 (2011).

[38] J. M. Yao, B. Bally, J. Engel, R. Wirth, T. R. Roth, and H. Hergert, Phys. Rev. Lett. **124**, 232501 (2020).

[39] J. Brewer, A. Mazeliauskas, and W. van der Schee, Phys. Rev. Lett. **127**, 242301 (2021).

[40] S. Acharya *et al.* (ALICE Collaboration), (2025), see also related results from ATLAS and CMS Collaborations, arXiv:2509.06428 [nucl-ex].

[41] W. Florkowski, A. Kumar, and R. Ryblewski, Progress in Particle and Nuclear Physics **108**, 103709 (2019), arXiv:1811.04409 [nucl-th].

[42] S. Bhadury, W. Florkowski, A. Jaiswal, A. Kumar, and R. Ryblewski, European Physical Journal Special Topics **230**, 655 (2021), arXiv:2101.11964 [nucl-th].

[43] E. Speranza and N. Weickgenannt, European Physical Journal A **57**, 155 (2021), arXiv:2007.00138 [nucl-th].

[44] X.-G. Huang, Nuclear Science and Techniques **36**, 208 (2025), arXiv:2411.11753 [nucl-th].

[45] E. Wigner, Phys. Rev. **51**, 106 (1937).

[46] T. Sogo, G. Ropke, and P. Schuck, Phys. Rev. C **79**, 051301 (2009), arXiv:0901.0675 [nucl-th].

[47] A. Tohsaki, H. Horiuchi, P. Schuck, and G. Röpke, Phys. Rev. Lett. **87**, 192501 (2001).

[48] J. S. Moreland, J. E. Bernhard, and S. A. Bass, Phys. Rev. C **92**, 011901 (2015), arXiv:1412.4708 [nucl-th].

[49] J. S. Moreland, J. E. Bernhard, and S. A. Bass, Phys. Rev. C **101**, 024911 (2020), arXiv:1808.02106 [nucl-th].

[50] D. Soeder, W. Ke, J. F. Paquet, and S. A. Bass, (2023), arXiv:2306.08665 [nucl-th].

[51] M. L. Miller, K. Reygers, S. J. Sanders, and P. Steinberg, Ann. Rev. Nucl. Part. Sci. **57**, 205 (2007), arXiv:nucl-ex/0701025 [nucl-ex].

[52] B. Alver *et al.*, Phys. Rev. C **77**, 014906 (2008), arXiv:0711.3724 [nucl-ex].

[53] S. Navas *et al.* (Particle Data Group), Phys. Rev. D **110**, 030001 (2024).

[54] G. e. a. A. C. Aad, Phys. Rev. Lett. **123**, 042001 (2019), arXiv:1903.07570 [hep-ex].

[55] A. M. e. a. C. C. Sirunyan, Nature **622**, 71 (2023), arXiv:2303.06046 [hep-ex].

[56] F. Becattini and M. A. Lisa, Annual Review of Nuclear and Particle Science **70**, 395 (2020).

[57] N. Weickgenannt, E. Speranza, D. Wagner, Q. Wang, and D. H. Rischke, Physical Review D **105**, 116026 (2022), arXiv:2203.04766 [hep-ph].

[58] M. Hongo, X.-G. Huang, M. Kaminski, M. Stephanov, and H.-U. Yee, Journal of High Energy Physics **11**, 150 (2021), arXiv:2107.14231 [hep-th].

[59] T. A. Lähde and U.-G. Meißner, *Nuclear Lattice Effective Field Theory: An Introduction*, Lecture Notes in Physics, Vol. 957 (Springer, 2019).

[60] G. Giacalone *et al.*, Phys. Rev. Lett. **135**, 012302 (2025), arXiv:2402.05995 [nucl-th].

[61] N. Summerfield, B.-N. Lu, C. Plumberg, D. Lee, J. Noronha-Hostler, and A. Timmins, Phys. Rev. C **104**, L041901 (2021), arXiv:2103.03345 [nucl-th].

[62] Y. Yamaguchi, W. Horiuchi, and N. Itagaki, Phys. Rev. C **108**, 014322 (2023), arXiv:2301.09839 [nucl-th].

[63] R. Bijker and F. Iachello, Nucl. Phys. A **1006**, 122077 (2021), arXiv:2011.01976 [nucl-th].

[64] H. Mehrabpour, arXiv preprint (2025), arXiv:2506.12673 [nucl-th].

[65] Y. Yamaguchi, W. Horiuchi, and N. Itagaki, Phys. Rev. C **108**, 014322 (2023), arXiv:2305.09182 [nucl-th].

[66] W. Li, W.-X. Zhou, and Y.-G. Ma, arXiv preprint (2025), arXiv:2504.04688 [nucl-th].

[67] H. D. Vries, C. W. D. Jager, and C. D. Vries, At. Data Nucl. Data Tables **36**, 495 (1987).

[68] S. Adachi and Y. Kanada-En'yo, Phys. Lett. B **818**, 136344 (2021), arXiv:2010.12484 [nucl-th].

[69] K. Shafi and S. Chatterjee, (2025), arXiv:2505.11713 [nucl-th].

[70] Y. Wang, S. Zhao, B. Cao, H.-j. Xu, and H. Song, Phys. Rev. C **109**, L051904 (2024), arXiv:2401.15723 [nucl-th].

[71] Z. Drogosz, W. Florkowski, and M. Hontarenko, Phys. Rev. D **110**, 096018 (2024), arXiv:2408.03106 [hep-ph].

[72] W. Ke, (2025), arXiv:2509.09549 [nucl-th].

[73] C. Zhang and J. Jia, Phys. Rev. Lett. **128**, 022301 (2022).

[74] W. Florkowski, B. Friman, A. Jaiswal, R. Ryblewski, and E. Speranza, Physical Review C **97**, 041901 (2018), arXiv:1705.00587 [nucl-th].

Appendix A: Derivation of the spin–correlation observable

In this appendix, we outline the derivation of the relation between the Λ -pair spin-correlation observable v_Λ^2 and the event-by-event polarization variance $\langle \mathcal{P}^2 \rangle$, following the formalism of Ref. [17].

The decay of a single polarized hyperon $\Lambda \rightarrow p\pi$ in its rest frame reads

$$\frac{dN}{d\Omega_p} \propto 1 + \alpha_\Lambda \mathbf{P} \cdot \hat{\mathbf{p}}_p. \quad (\text{A1})$$

For a pair of hyperons (1,2) this gives

$$\frac{d^4 N}{d\Omega_1 d\Omega_2} \propto (1 + \alpha_1 \mathbf{P}_1 \cdot \hat{\mathbf{k}}_1)(1 + \alpha_2 \mathbf{P}_2 \cdot \hat{\mathbf{k}}_2), \quad (\text{A2})$$

which we rewrite in the general form

$$\frac{d^4 N}{d\Omega_1 d\Omega_2} \propto 1 + \alpha_1 \mathbf{P}_1 \cdot \hat{\mathbf{k}}_1 + \alpha_2 \mathbf{P}_2 \cdot \hat{\mathbf{k}}_2 + \sum_{i,j} C_{ij} \hat{k}_1^i \hat{k}_2^j, \quad (\text{A3})$$

where C_{ij} encodes all two-body spin correlations up to bilinear order in $\hat{\mathbf{k}}_{1,2}$.

We focus on the relative angle

$$\cos \Delta\theta \equiv \hat{\mathbf{k}}_1 \cdot \hat{\mathbf{k}}_2. \quad (\text{A4})$$

From Eq. (A3) one finds

$$\langle \cos \Delta\theta \rangle \equiv \frac{\int d\Omega_1 d\Omega_2 \frac{d^4 N}{d\Omega_1 d\Omega_2} (\hat{\mathbf{k}}_1 \cdot \hat{\mathbf{k}}_2)}{\int d\Omega_1 d\Omega_2 \frac{d^4 N}{d\Omega_1 d\Omega_2}} = \frac{1}{9} \text{Tr}(C), \quad (\text{A5})$$

using $\int d\Omega \hat{k}^i = 0$ and $\int d\Omega \hat{k}^i \hat{k}^j = \frac{4\pi}{3} \delta^{ij}$.

Rotational invariance and the truncation to bilinear structures imply that the one-dimensional distribution in $\cos \Delta\theta$ must be linear,

$$\frac{dN}{d \cos \Delta\theta} \propto 1 + D \cos \Delta\theta, \quad (\text{A6})$$

so that

$$\langle \cos \Delta\theta \rangle = \frac{D}{3}. \quad (\text{A7})$$

Combining with Eq. (A5) gives

$$D = \frac{1}{3} \text{Tr}(C) = 3 \langle \cos \Delta\theta \rangle. \quad (\text{A8})$$

In the model used in this work, the fireball in a given event carries a global polarization $\mathcal{P} = \mathcal{P} \hat{\mathbf{n}}$, shared by all produced Λ hyperons (local nonflow-like correlations can be reduced by an η -gap cut). Thus

$$\mathbf{P}_1 = \mathbf{P}_2 = \mathcal{P}, \quad (\text{A9})$$

and comparison with the product form yields

$$C_{ij} = \alpha_1 \alpha_2 \mathcal{P}_i \mathcal{P}_j, \quad (\text{A10})$$

so that

$$\langle \cos \Delta\theta \rangle = \frac{D}{3} = \frac{1}{9} \text{Tr}(C) = \frac{\alpha_1 \alpha_2}{9} \mathcal{P}^2. \quad (\text{A11})$$

Event averaging (double brackets) finally gives

$$v_\Lambda^2 \equiv \frac{9}{\alpha_1 \alpha_2} \langle \langle \cos \Delta\theta \rangle \rangle = \langle \mathcal{P}^2 \rangle. \quad (\text{A12})$$

For $\Lambda\bar{\Lambda}$ and $\bar{\Lambda}\bar{\Lambda}$ pairs one only needs to use the corresponding values (and signs) of the decay parameters α_1 and α_2 .

Appendix B: Relativistic spin hydrodynamics

This appendix summarizes the basic structure of relativistic spin hydrodynamics and fixes the notation used in Sec. II A, following Refs. [17, 41, 43, 74].

The equations of motion are given by the conservation of energy–momentum and total angular momentum [58, 74],

$$\partial_\mu T^{\mu\nu} = 0, \quad \partial_\lambda J^{\lambda,\mu\nu} = 0, \quad (\text{B1})$$

where $T^{\mu\nu}$ is the energy–momentum tensor and $J^{\lambda,\mu\nu}$ the total angular-momentum tensor. The latter can be decomposed into orbital and spin contributions,

$$J^{\lambda,\mu\nu} = L^{\lambda,\mu\nu} + S^{\lambda,\mu\nu}, \quad L^{\lambda,\mu\nu} = x^\mu T^{\lambda\nu} - x^\nu T^{\lambda\mu}. \quad (\text{B2})$$

Inserting this decomposition into Eq. (B1) and using $\partial_\mu T^{\mu\nu} = 0$ one obtains

$$\partial_\lambda S^{\lambda,\mu\nu} = T^{\nu\mu} - T^{\mu\nu}, \quad (\text{B3})$$

which shows that the spin tensor $S^{\lambda,\mu\nu}$ is exactly conserved only if the energy–momentum tensor is symmetric. Different pseudo-gauge choices correspond to different decompositions of $T^{\mu\nu}$ and $S^{\lambda,\mu\nu}$, but leave the total charges associated with $J^{\lambda,\mu\nu}$ invariant [57, 58].

It is convenient to introduce the spin-density tensor

$$S^{\mu\nu} \equiv u_\lambda S^{\lambda,\mu\nu}, \quad (\text{B4})$$

where u^μ is the fluid four-velocity. Among the six independent components of $S^{\mu\nu}$ one can define the “magnetic” spin-density four-vector

$$S^\mu \equiv \frac{1}{2} \epsilon^{\mu\nu\alpha\beta} S_{\nu\alpha} u_\beta, \quad S^\mu u_\mu = 0, \quad (\text{B5})$$

which contains three independent spatial components in the local rest frame. In ideal spin hydrodynamics the independent hydrodynamic fields are the energy density, the fluid four-velocity u^μ , and the antisymmetric spin potential $\Omega^{\mu\nu}$, thermodynamically conjugate to $S^{\mu\nu}$; the relation between $S^{\mu\nu}$ and $\Omega^{\mu\nu}$ is specified by an equation of state.

In the initial state of a high-energy nuclear collision we assume boost invariance around midrapidity and vanishing transverse flow, so that $u^\mu = (1, 0, 0, 0)$ at $\tau \rightarrow 0^+$. Following Ref. [17], only the spatial components of S^μ are taken

to be nonzero initially and are parameterized as $S^i = n^i S$, with a unit vector n^i defining the random orientation of the event-wise polarization and a scalar amplitude S , see Eq. (1). The corresponding initial spin density per unit rapidity at midrapidity, Eq. (2), is implemented in our model through the smeared participant sum $\mathcal{S}(\mathbf{x})$ in Eq. (3), which provides a concrete realization of $S(\mathbf{x})$ that can be used as input for spin-hydrodynamic simulations.

Appendix C: Polarization variance and scaled spin fluctuations

In this appendix we collect the relations between the event-by-event polarization variance, spin–spin correlations in the colliding nuclei, and the baseline and scaled observables used in the main text.

The event-wise polarization is defined in Eq. (13) as

$$\mathcal{P} = \frac{1}{N_{\text{part}}} \left(\sum_{i=1}^{N_{\text{part}}^A} s_{i,A} + \sum_{j=1}^{N_{\text{part}}^B} s_{j,B} \right), \quad N_{\text{part}} = N_{\text{part}}^A + N_{\text{part}}^B, \quad (\text{C1})$$

where $s_{i,A} = \pm 1$ and $s_{j,B} = \pm 1$ denote spin projections of participants from nuclei A and B , respectively. For unpolarized colliding ions the one-body spin density is symmetric, so that $\langle s_{i,A} \rangle = \langle s_{j,B} \rangle = 0$ and $\langle \mathcal{P} \rangle = 0$.

The variance of \mathcal{P} in a given centrality class is

$$\langle \mathcal{P}^2 \rangle = \frac{1}{N_{\text{part}}^2} \left\langle \left(\sum_{i=1}^{N_{\text{part}}^A} s_{i,A} + \sum_{j=1}^{N_{\text{part}}^B} s_{j,B} \right)^2 \right\rangle. \quad (\text{C2})$$

Because spin degrees of freedom in the two nuclei are independent, the mixed terms factorize and vanish,

$$\langle s_{i,A} s_{j,B} \rangle = \langle s_{i,A} \rangle \langle s_{j,B} \rangle = 0, \quad (\text{C3})$$

and one obtains

$$\langle \mathcal{P}^2 \rangle = \frac{1}{N_{\text{part}}^2} \left[\sum_{i,k=1}^{N_{\text{part}}^A} \langle s_{i,A} s_{k,A} \rangle + \sum_{j,l=1}^{N_{\text{part}}^B} \langle s_{j,B} s_{l,B} \rangle \right]. \quad (\text{C4})$$

Consider, for definiteness, the contribution from nucleus A . It contains N_{part}^A diagonal terms with $i = k$ and $N_{\text{part}}^A(N_{\text{part}}^A - 1)$ off-diagonal terms with $i \neq k$,

$$\begin{aligned} \sum_{i,k=1}^{N_{\text{part}}^A} \langle s_{i,A} s_{k,A} \rangle &= N_{\text{part}}^A \sum_{s=\pm 1} \rho_A^{(1)}(s) s^2 \\ &+ N_{\text{part}}^A(N_{\text{part}}^A - 1) \sum_{s_1, s_2 = \pm 1} \rho_A^{(2)}(s_1, s_2) s_1 s_2, \end{aligned} \quad (\text{C5})$$

where $\rho_A^{(1)}(s)$ is the one-body spin density of participants from nucleus A , and $\rho_A^{(2)}(s_1, s_2)$ is the two-body spin density defined nucleus A . An analogous expression holds for nucleus

B . Inserting Eq. (C5) (and its B counterpart) into Eq. (C4) yields

$$\begin{aligned} \langle \mathcal{P}^2 \rangle &= \frac{1}{N_{\text{part}}^2} \left[N_{\text{part}}^A \sum_s \rho_A^{(1)}(s) s^2 \right. \\ &+ N_{\text{part}}^A(N_{\text{part}}^A - 1) \sum_{s_1, s_2} \rho_A^{(2)}(s_1, s_2) s_1 s_2 \\ &+ N_{\text{part}}^B \sum_s \rho_B^{(1)}(s) s^2 \\ &\left. + N_{\text{part}}^B(N_{\text{part}}^B - 1) \sum_{s_1, s_2} \rho_B^{(2)}(s_1, s_2) s_1 s_2 \right]. \end{aligned} \quad (\text{C6})$$

For collisions of identical nuclei one has $\rho_A^{(n)} = \rho_B^{(n)}$ and Eq. (C6) reduces, up to an overall normalization factor, to the schematic relation (14) given in the main text. The dependence on the one-body densities $\rho^{(1)}$ reflects the trivial variance of independent spins, while the terms containing $\rho^{(2)}$ encode genuine two-body spin–spin correlations, such as those induced by α clustering.

To isolate nontrivial spin structures, it is useful to construct a baseline that only contains the global $J = 0$ constraint of the nuclear ground state. Consider a single nucleus with mass number A_{mass} and spin variables $s_i = \pm 1$. Total angular momentum conservation implies

$$\sum_{i=1}^{A_{\text{mass}}} s_i = 0. \quad (\text{C7})$$

Squaring this relation and taking an expectation value gives

$$\begin{aligned} 0 &= \left\langle \left(\sum_{i=1}^{A_{\text{mass}}} s_i \right)^2 \right\rangle \\ &= A_{\text{mass}} \langle s_i^2 \rangle + A_{\text{mass}}(A_{\text{mass}} - 1) \langle s_i s_j \rangle_{\text{base}}, \end{aligned} \quad (\text{C8})$$

where $\langle s_i^2 \rangle = 1$ and, by symmetry, all distinct pairs $(i \neq j)$ have the same correlation $\langle s_i s_j \rangle_{\text{base}}$. Solving for this pair correlation one finds

$$\langle s_i s_j \rangle_{\text{base}} = -\frac{1}{A_{\text{mass}} - 1}, \quad (\text{C9})$$

which is the “trivial” negative background correlation quoted in the main text.

Now consider a collision between nuclei A and B and restrict attention to participants. Assuming that the intrinsic pair correlation between any two nucleons from the same nucleus is given by the value in Eq. (C9), independent of whether the nucleons participate in the reaction, the baseline variance of the polarization follows from Eq. (C4). For each nucleus the diagonal and off-diagonal contributions read

$$\sum_{i,k=1}^{N_{\text{part}}^A} \langle s_{i,A} s_{k,A} \rangle_{\text{base}} = N_{\text{part}}^A + N_{\text{part}}^A(N_{\text{part}}^A - 1)c, \quad (\text{C10})$$

and similarly for nucleus B . We have $N_{\text{part}}^A = N_{\text{part}}^B$, the resulting baseline variance is

$$\begin{aligned}\langle \mathcal{P}^2 \rangle_{\text{base}} &= \frac{1}{N_{\text{part}}^2} \left[N_{\text{part}}^A + N_{\text{part}}^B \right. \\ &\quad \left. + c N_{\text{part}}^A (N_{\text{part}}^A - 1) + c N_{\text{part}}^B (N_{\text{part}}^B - 1) \right] \\ &= \frac{1}{N_{\text{part}}^2} \left[N_{\text{part}} + c N_{\text{part}} (N_{\text{part}}/2 - 1) \right],\end{aligned}\quad (\text{C11})$$

which is equivalent to Eq. (16) used in Sec. II C. By construction, this quantity encodes only the global $J = 0$ constraint and contains no information on additional local spin–spin structures.

Since $\langle \mathcal{P} \rangle = 0$, the standard deviation of the polarization is simply

$$\text{std}(\mathcal{P}) = \sqrt{\langle \mathcal{P}^2 \rangle}. \quad (\text{C12})$$

Accordingly, the scaled standard deviation plotted in Sec. III is defined as

$$(\sqrt{\langle \mathcal{P}^2 \rangle})_{\text{scaled}} = \frac{\sqrt{\langle \mathcal{P}^2 \rangle}}{\sqrt{\langle \mathcal{P}^2 \rangle}_{\text{base}}}, \quad (\text{C13})$$

which equals unity for the purely baseline correlations and deviates from unity only in the presence of nontrivial spin structures beyond the global $J = 0$ constraint.

Appendix D: Processing of NLEFT configurations

This appendix briefly summarizes how the *ab initio* NLEFT configurations are used as input to the our model simulations of Sec. III.

For each nucleus considered in this work, NLEFT provides an ensemble of ground-state configurations generated on a spacetime lattice with chiral effective interactions. Each configuration consists of the three-dimensional coordinates of all

nucleons and their spin–isospin quantum numbers, sampled with the pinhole algorithm, so that many-body correlations in both coordinate and spin–isospin space are preserved.

In order to use these configurations as nuclear-structure input for T_RENTo:

- For each event, one NLEFT configuration is chosen at random for nucleus A and one (independently) for nucleus B .
- For each chosen configuration, the center-of-mass position is shifted to the origin, and a random global spatial rotation is applied to generate an isotropic orientation of the intrinsic nuclear shape relative to the beam axis.
- The rotated coordinates are then projected onto the transverse plane to provide the initial positions \mathbf{x}_i of the nucleons in T_RENTo, while the longitudinal coordinates are used only to ensure that no artificial correlations along the beam direction are introduced.
- The spin projection $s_i = \pm 1$ assigned to each nucleon in the main text is inherited from the NLEFT configuration by choosing a quantization axis in the body-fixed frame of the nucleus and mapping the corresponding spin eigenvalues onto ± 1 . This procedure preserves the local spin–spin correlations encoded in the NLEFT ensemble.

The two-nucleon spin-correlation function shown in Fig. 1 is obtained by averaging the product $s_i s_j$ over all pairs of nucleons in the NLEFT ensemble and binning the results as a function of their relative distance $\delta r = |\mathbf{x}_i - \mathbf{x}_j|$. The same configurations, after random rotations and shifts as described above, are then used as nuclear-structure input to generate the initial conditions of T_RENTo events and to compute the event polarizations \mathcal{P}_{ini} and their fluctuations for $^{16}\text{O} + ^{16}\text{O}$ and $^{20}\text{Ne} + ^{20}\text{Ne}$ collisions.